DOE/ER/60642--T1

Positron Ring System Using Anger-type Detectors

Progress Report

February 15, 1992 to July 31, 1992

and

Incremental Funding Request

February 15, 1993 to February 14, 1994

Joel S. Karp, Ph.D.

The University of Pennsylvania
3400 Spruce St.
Philadelphia, PA 19104

August 1, 1992

Prepared for the U.S. Department of Energy

Grant No. DE-FG02-88ER60642

DOE/ER/60642-4

Abstract

The major accomplishments this year, so far, are 1) validation of Monte Carlo simulation code with scattered, as well as true coincidences, for a variety of scanner geometries, 2) validation of 3-D reprojection-reconstruction algorithm and comparisons to 2-D reconstruction, as a function of the scanner axial extent, using simulated data, 3) initial development of energy window scatter correction technique for use in volume imaging PET, 4) evaluation of high-countrate calibrations and imaging of ^{15}O brain studies with the UGM PENN-PET.

Progress Report

1. Crystal experiments

We have continued to pursue experimentation on NaI(Tl) crystals in the glove box, where we can handle unencapsulated crystals. By the end of 1991, we had investigated several methods of extending the active areas of the detector, in order to minimize the amount of missing data at the edges of the detectors [1]. These methods included 1) optically coupling the neighboring detectors directly to each other, 2) various arrangements of the photomultiplier tubes (PMTs) used to read out the scintillation light, and 3) surface treatment of the edges and front face of the crystal to improve and focus overall light collection and hence position resolution. Of these three methods, both 2) and 3) led to measurable improvements in positioning events near the edge of the crystal. In addition, they are both practical methods to implement.

Since then, we have also investigated a different method of modifying the front surface. We have used and evaluated a pattern of grooves on the front surface, uniformly over the entire face, to restrict the spread of light. After experimenting with different machining techniques, we are now adding a pattern of slots near the edge, in order to preferentially direct the light toward the edge of the crystal. This is similar to the concept of BGO block detectors. Our preliminary data shows that this method can further extend the active area of the detector without introducing discontinuities, and while retaining a simple centroid position algorithm. We will experiment with the depth and placement of slots, to optimize the configuration for NaI(Tl), which inherently has higher light output than BGO, while continuing to use our relatively large 50-mm wide PMTs.

2. Monte Carlo Simulation

The Monte Carlo program was changed to allow us to easily modify the scanner geometry, so that we could simulate our present proto-type PENN-PET scanner (axial FOV = 9 cm, transverse FOV = 51.2 cm), our UGM PENN-PET scanner (axial FOV = 12.8 cm, transverse FOV = 51.2 cm), a large axial FOV whole body system (axial FOV = 25.6 cm, transverse FOV = 51.2 cm), and a large axial FOV head system (axial FOV = 25.6 cm, transverse FOV = 25.6 cm). We are validating the program by comparing it to experimental data that has been acquired with the two existing PENN-PET scanners, with 9-cm and 12.8-cm axial extents [2]. The program allows the user to choose an input activity distribution (including points, cylinders, 3-D brain phantom) and scatter medium, so that one can separately investigate the true and scatter coincidences. Random coincidences are currently being included in the program. The program can also vary the detector spatial and energy resolution. Compton scattering in the detector, as well as depth-of-interaction are currently being added to the program. Although

we have only simulated NaI(Tl) detectors so far, the detector scintillator in the program can be varied. The program outputs list-mode data, so that we can reconstruct the same data with both 2-D and 3-D reconstruction algorithms. These include the 2-D single-slice rebinning algorithm [3], the 3-D reprojection-reconstruction algorithm [4], and the 3-D multi-slice rebinning algorithm [5].

3. 3-D reconstruction algorithm - simulations

The 3-D reprojection-reconstruction algorithm [4] has been tested and evaluated with ideal data (no tissue scatter and perfect detector resolution), provided by the Monte Carlo simulation program. There are several questions that arise when trying to increase sensitivity by increasing the axial extent of a volume imaging PET scanner without septa. One important question that we have studied is whether or not a 3-D reconstruction algorithm offers a significant gain in performance over a 2-D reconstruction algorithm, and also how this potential gain changes as a function of the axial extent (and acceptance angle) of the scanner [5]. Since we built the PENN-PET scanner, we have always acquired data without septa and with a relatively large acceptance angle, but have used a 2-D reconstruction algorithm, rather than a 3-D algorithm, because the 2-D algorithm offers advantages in speed, practicality, and validation of quantitative corrections of detector normalization, scatter and randoms, and attenuation. As seen in Fig.1, a larger acceptance angle leads to an improvement in statistics and commensurate reduction in noise, particularly near the axial center. The 2-D algorithm, however, leads to a loss in spatial resolution, particularly in the axial direction, for off-center points, as seen in Fig.2. The loss in axial resolution is also demonstrated using a multiple disk phantom, as seen in Fig.3, where the contrast between disks of activity is reduced as the acceptance angle increases, when using the 2-D algorithm. With the 3-D algorithm, the spatial resolution in the axial direction is preserved.

A comparison was also made using a simulation of a realistic 3-D brain (digital representation of the Data Spectrum phantom, provided by E. Hoffman, UCLA). As shown in Fig.4, the RMS difference from the base image is plotted as a function of reconstruction algorithm and acceptance angle, for regions in the image representing the outer cortical structures and the inner sub-cortical structures. The base image is a calculated forward projection and reconstruction of the 3-D brain phantom. There is a significant decrease in the RMS difference with the 2-D algorithm with a larger (9 degree) acceptance angle compared to the smaller (1 degree) acceptance angle, because of the increase in statistics. There is only a small additional improvement in the RMS difference with the 3-D algorithm over the 2-D algorithm, with the large acceptance angle. The full acceptance angle of 9 degrees corresponds to the standard geometry of the UGM PENN-PET scanner, a whole body scanner with a 12.8-cm axial FOV.

A second comparison between the 2-D and 3-D algorithms was made using

the geometry of the proposed HEAD scanner, as illustrated in Fig.5, which will have a full acceptance angle of 26 degrees. Fig.6 shows the expected improvement in statistics and reduction in noise, with this geometry compared to the present geometry. Fig.7 shows the RMS difference from the base image of the 3-D brain phantom simulations for the 2-D reconstruction algorithm, for 9, 18, and 26 degree angular acceptance, and for the 3-D algorithm with full angular acceptance. With low imaging statistics (3 million total), the larger angular acceptance leads to an improvement in image quality, even with the 2-D algorithm. With better imaging statistics (42 million total), the image quality degrades with the larger angular acceptance for the 2-D algorithm (because of the degradation in spatial resolution) and is best with the 3-D algorithm.

Our preliminary conclusions from these simulations are that for our present geometry (angular acceptance of 9 degrees) the 2-D reconstruction (single-slice rebinning) is essentially as accurate as 3-D reconstruction for realistic brain imaging, especially in the center of the transverse FOV. For large axial extent scanners, some form of 3-D reconstruction is required to retain accuracy while taking full advantage of the increased sensitivity. In addition, the physical sources of error, which have not yet been simulated, will need to be accurately compensated for in the 3-D algorithm, in order to retain its gain in performance over the 2-D algorithm.

4. Large field-of-view scanner geometry - simulations

We have incorporated the physical effects of scatter and attenuation in the Monte Carlo program, in order to predict the performance of the HEAD scanner that we are designing. The advantage of using NaI(Tl) in volume imaging is the very good energy resolution, which is 10% (FWHM) with pulse clipping and 240 ns integration, and 8% (FWHM) without pulse clipping and full integration of 1μs. Fig. 8 shows a simulated energy spectra (with the assumption of 10% resolution) of both true and scattered events, for a head-sized cylinder (18-cm diameter, 10-cm long). This simulation includes the effect of Compton scatter in the detector. Also shown is the measured scatter fraction for the proto-type scanner, as a function of energy threshold, showing the reduction in scatter fraction as the threshold is raised. Typically, we operate at 450 keV, which results in a scatter fraction of about 13%. The scatter fraction is about the same for both the proto-type and UGM scanners, despite the large axial extent of the UGM scanner. We are concerned, however, about the potential increase in scatter for a scanner with a very large axial extent, without septa, and have therefore used the Monte Carlo program to simulate data for a variety of scanner geometries.

Fig.9 shows the predicted scatter fraction at 450 keV for the proto-type PENN-PET scanner geometry, with a full angular acceptance of 6.5 degrees, and for a large axial FOV scanner geometry (whole-body), with a full angular

acceptance of 16 degrees. The scatter fraction does not increase for the larger scanner, with an energy threshold of 450 keV. Here the value of the scatter fraction is about 25%, which is larger than our measured value, because the simulation counts all scattered events above 450 keV, even those at 510 keV, which in reality are indistinguishable from true 511 keV photopeak events. This preliminary data confirms that we should not expect the scatter fraction to increase for a scanner with a larger axial extent, as long as we use a tight energy window. This conclusion, however, may depend on the diameter of the system, and so we will next investigate the HEAD scanner geometry, which has a 25.6-cm axial extent, but only half the diameter (42-cm) of the whole-body PENN-PET systems (84-cm).

5. Scatter correction in volume imaging PET

Most previous scattering correction techniques in PET are based on deconvolution methods using measured scattering response functions. As an alternative method to compensate for in-plane as well as out-of-plane scatter, which is more prevalent in volume imaging systems without septa, we are investigating an energy correction method. This method potentially can be relatively fast, simple, and less dependent on prior calibration measurements. In addition, it should compensate for both scatter out-of-plane as well as out-of-the-FOV. A triple-window energy method will use the counts both directly below and above the photopeak (of both coincident detectors) to estimate the scatter under the photopeak.

The Monte Carlo program which can simulate a variety of phantoms, with scatter, is being used to develop and evaluate the technique. Fig. 10 shows a comparison of the simulated scatter (which is known from the program) and the estimated scatter (which is determined from the simulated total using the energy correction method) for two activity distributions. There is good agreement for both cases. Although this method does depend on a position-dependent calibration factor, which is calculated prior to the study, the factor was not varied for the two cases shown, indicating that a single calibration may be sufficient for a wide range in studies. This will be further investigated with a larger variety of activity distributions.

6. Quantitation and high-countrate calibrations

Over the past year we have been performing a variety of studies on the UGM scanner, as well as the proto-type scanner, which has been in operation for over five years. A number of patients having ^{18}F-FDG brain studies were imaged sequentially on both scanners, in order to confirm that the two scanners give comparable quantitative results. The extended axial FOV of the UGM scanner is clearly advantageous, particularly since the PET images are often

matched with an MRI image of the same patient. The UGM scanner, with its faster electronics and high-countrate capability, is also regularly used for ^{15}O-H_2O stimulation studies. Since the PENN-PET is a septum-less volume imaging scanner it has a high sensitivity to activity. However, because of the use of continuous detectors and the single position calculator, the system saturates at a relatively low activity concentration. Therefore, we have designed, at the University of Pennsylvania, an imaging protocol for ^{15}O brain activation studies which optimizes the counting statistics with a short imaging time. Rather than injecting a very short bolus of high activity, which leads to countrate limitations of the scanner, a slow bolus technique is being used, where 40 mCi is injected at a relatively constant rate over 3.5 minutes, and the data are collected dynamically in 10-20 second frames, starting 0.5 minutes after the beginning of infusion. Most of the data are then collected near the peak of the countrate capability, which is between 0.6 and 1.0 μCi/cc.

The deadtime becomes appreciable for the UGM scanner above an activity concentration of 0.5 μCi/cc. At this point, the average singles countrate in each of the six detectors is about 1,500,000 CPS while the total coincident countrate (input to the processing electronics) is about 350,000 CPS. As seen in Fig.11, the true countrate which is recorded, after energy gating, scatter, and randoms subtraction, is a maximum of about 50,000 CPS. Presently, we calibrate the deadtime as a function of the detector's singles countrates by using a known (cylinder phantom) distribution of activity [7]. This calibration is valid over a wide range of cylinder sizes, encompassing the normal variation in brain sizes, as shown in Fig.12. The deadtime for a patient study is calculated from a lookup table generated from the phantom data. Fig.13 shows the good agreement between the true activity concentration and measured concentration of a realistic 3-D brain phantom, after all quantitative corrections, including deadtime.

Future Plans

For the remainder of this year, and for next year, we plan to work on the following projects.

The work on the crystals in the glove box will continue. This has two major purposes. The first is that we wish to minimize the dead space at the edge of the detector, and the second is that we wish to improve the spatial resolution resolution of the detector. These goals can be achieved through a variety of surface treatments and PMT configurations. Some of these methods will be applied to the single cylindrical crystal that we are designing (which is being manufactured by Bicron) and some may be applied to future detector designs, which may again be modular in design. In addition, we will experiment with pure NaI, which if cooled, has high light output and a fast decay time. For example, at -188 degrees Celsius, the light decay time is about 62 ns, compared to

240 ns for NaI(Tl) at room temperature, and with our delay-line clipping technique, the usable light output would be twice that of NaI(Tl). This would then lead to better energy resolution, better position resolution, and higher countrate capability due to the reduction in pulse pileup. At -100 degrees Celsius, the decay time of pure NaI is 32 ns leading to even better timing, with about the same light output as NaI(Tl) at room temperature. We expect to spend a significant amount of time first learning how to cool and couple the crystal at low temperatures, before studying the best tradeoffs in performance and practicality.

The Monte Carlo simulation will continue to be further developed. We will add the effect of random coincidences and the capability of 'collecting' data in singles mode. In addition, the detector effects of Compton scatter and the uncertainty of the depth-of-interaction will be fully incorporated into the code, in order to more realistically simulate real data.

The 3-D reprojection-reconstruction algorithm has been tested with ideal simulated data, but not fully with real data. We need to incorporate detector normalization, scatter and randoms subtraction, and attenuation correction in the 3-D algorithm. We have developed methods which are extensions of the methods used in our 2-D algorithm, but have not yet fully included them, nor tested them with the 3-D algorithm. This will be done with both the simulation, where the effects can be isolated, and with real data, where the effects are cumulative. In addition, we will evaluate the 3-D multi-slice algorithm, and compare it to the 3-D reprojection-reconstruction algorithm, to see whether the geometrical approximations in either algorithm lead to loss of image quality. Again, this can be done both with simulations and with real data.

We will use the Monte Carlo program to simulate the HEAD scanner geometry, in terms of energy and spatial resolution, sensitivity, scatter, and randoms. These predictions should help us better understand the imaging tradeoffs in PET with a large angular acceptance. In effect, the program can be used to investigate whether there are limitations in extending the axial extent of the scanner, and what the potential gain is.

Since scattered radiation is a large consideration in volume imaging, particularly as we increase the axial extent, we need to consider better methods of scatter correction. We have previously evaluated background subtraction methods, 1-D and 2-D deconvolution methods, and will continue this year to pursue energy correction methods.

There is no question that the present PENN-PET design is somewhat limited by it relatively low countrate capability, compared to multi-crystal BGO scanners. There are many areas, however, that potentially can be further improved with our design. The first area is to improve the front-end signal processing, through a variety of preamplifier and cable improvements. The second is to reduce the number of events that are processed by the position calculator, and which are afterwards thrown away. This can be done by shielding the detectors from very low-energy gamma rays, and by implementing a

hardware upper-level energy discriminator, in addition to the lower-level energy discriminator. A third area of investigation, which is critical for the cylindrical detector, is full implementation of local triggering and detector zones. The number of zones and amount of zone overlap need to be optimized. Finally, there are a number of improvements that can be made to speed up the position calculator, however, this is a project that UGM Medical Systems is pursuing.

Finally, we are expecting the cylindrical crystal to be delivered in the near future. We have a simple mechanical gantry built and a partial set of electronics debugged and tested. The poistion calculator will be added and tested this fall. With these electronics and available photo-multiplier tubes, we can set up about half of the required 180 channels. This will be sufficient to begin performance measurements, including spatial resolution, sensitivity and scatter, and countrate performance. We have also designed a computer-controlled rotating platter which can be used to image a variety of activity distributions, including cylinders and brain phantoms. Before imaging, however, we will first need to modify the methods of spatial distortion correction and detector normalization used for our present detectors, in order to account for the cylindrical geometry of the new crystal.

References

1. Freifelder RH, Haigh AT, Karp JS. *Reducing edge effects and improving position resolution in position-sensitive NaI(Tl) detectors.* Presented at the IEEE Medical Imaging Conference, 1991. (under review for publication in IEEE Trans Nucl Sci.).

2. Karp JS, Kinahan PE, Muehllehner G, Countryman P. *Effect of increased axial field of view on the performance of a volume PET scanner.* Presented at the IEEE Medical Imaging Conference, 1991. (accepted for publication in IEEE Trans Med Imaging).

3. Daube-Witherspoon, Muehllehner G. *Treatment of axial data in three-dimensional PET.* J Nucl Med 28: 1717-1724, 1987.

4. Kinahan PE, Karp JS. *Three dimensional image reconstruction by reprojection.* Proceedings of the 12th annual international conference of the IEEE Engineering in Medicine and Biology Society, 1990.

5. Lewitt RM, Muehllehner G, Karp JS. *3D image reconstruction for PET by multi-slice rebinning and axial filtering.* Presented at the IEEE Medical Imaging Conference, 1991. (in preparation)

6. Kinahan PE, Karp JS. *Image reconstruction for volume-imaging PET as a function of axial extent: A Monte Carlo study.* Presented at the Society of Nuclear Medicine Conference, 1992. J Nucl Med 33: 871 (abstract).

7. Smith R, Karp JS, Countryman PJ, Muehllehner G. *Countrate performance of a septum-less volume imaging scanner.* Presented at the Society of Nuclear Medicine Conference, 1992. J Nucl Med 33: 861 (abstract).

Publications since last progress report

1. Karp JS, Daube-Witherspoon ME, Hoffman EJ, et al. Performance Standards in Positron Emission Tomography. J Nucl Med 32: 2342-2350, 1991.

2. Karp JS, Muehllehner G. Standards for performance measurements of PET scanners: Evaluation with the UGM PENN-PET 240H scanner. Med Progress through Technology 17: 173-187, 1991.

3. Karp JS, Freifelder R. Current and future technological trends in Positron Emission Tomography. J Neuroimag 2: 102-110.

4. Karp JS, Kinahan PE, Muehllehner G, Countryman P. *Effect of increased axial field of view on the performance of a volume PET scanner.* (accepted for publication in IEEE Trans Med Imaging).

5. Freifelder RH, Haigh AT, Karp JS. *Reducing edge effects and improving position resolution in position-sensitive NaI(Tl) detectors.* (under review for publication in IEEE Trans Nucl Sci.).

6. Kinahan PE, Karp JS. *Image reconstruction for volume-imaging PET as a function of axial extent: A Monte Carlo study.* Presented at the Society of Nuclear Medicine Conference, 1992. J Nucl Med 33: 871 (abstract).

7. Smith R, Karp JS, Countryman PJ, Muehllehner G. *Countrate performance of a septum-less volume imaging scanner.* Presented at the Society of Nuclear Medicine Conference, 1992. J Nucl Med 33: 861 (abstract).

8. Countryman PJ, Smith RJ, Karp JS. *Attenuation correction in a volume imaging PET scanner.* Presented at the Society of Nuclear Medicine Conference, 1992. J Nucl Med 33: 862 (abstract).

Figure Captions

1. Simulated mean counts (top) and standard deviation (bottom) vs. axial position, for a uniform cylinder of activity, 18-cm diameter x 10-cm long, for the standard geometry of the UGM PENN-PET (axial FOV= 12.8 cm, diameter = 84 cm). The full acceptance angle of the UGM scanner is 9 degrees.

2. Simulated axial profiles at r = 0 mm (top) and r = 100 mm (bottom) for both the 2-D reconstruction algorithm, with limited 1 degree and full 9 degree angular acceptance, and the 3-D reconstruction algorithm with the full 9 degree angular acceptance.

3. Simulated axial profiles of disk phantom, which has alternating 12-mm thick disks of activity with 12-mm thick disks of no activity. The data was reconstructed with the 2-D reconstruction algorithm, with limited 1 degree and full 9 degree angular acceptance, and the 3-D reconstruction algorithm with the full 9 degree angular acceptance.

4. Simulations of the 3-D brain phantom were reconstructed with the 2-D and 3-D reconstruction algorithms and compared to the calculated forward-and-backprojection of the digital phantom (base image). The root-mean-square (rms) difference between the base image and reconstructed image was calculated for an outer region, representing the cortical area, and an inner region, representing the sub-cortical area, and globally, for the whole image.

5. Illustration of the standard geometry of the UGM PENN-PET scanner, and the proposed HEAD geometry with a very large axial extent.

6. Simulated mean counts (top) and standard deviation (bottom) vs. axial position, for a uniform cylinder of activity, 18-cm diameter x 10-cm long, for the standard geometry of the UGM PENN-PET (axial FOV= 12.8 cm, diameter = 84 cm) and the HEAD geometry (axial FOV = 25.6 cm, diameter = 42 cm). The full acceptance angle of the UGM scanner is 9 degrees, while that of the HEAD scanner is 26 degrees.

7. Simulations of the 3-D brain phantom were reconstructed with the 2-D and 3-D reconstruction algorithms and compared to the calculated forward-and-backprojection of the digital phantom (base image). The root-mean-square (rms) difference between the base image and reconstructed image was calculated globally, for the whole image.

8. Simulated energy spectra (top) for events which do not scatter (true) and which do scatter in the 18-cm x 10-cm cylinder of water. Compton scattering in

the NaI(Tl) detector is included. Also shown (bottom) are the measured scatter/true ratios, as a function of energy threshold, for the proto-type PENN-PET scanner.

9. Simulated true and scattered coincidences of 18-cm x 19-cm cylinder of activity for the whole-body proto-type PENN-PET scanner (axial FOV = 9 cm), and a whole-body scanner with a large axial FOV = 25.6 cm. The full angular acceptance of the proto-type scanner is 6.5 degrees, while that of the large FOV scanner is 16 degrees.

10. Simulated true and scattered coincidences, compared to estimated scatter using the multiple energy window scatter correction technique, for two distributions.

11. Coincidence countrates vs. activity for UGM PENN-PET scanner, using an 18-cm x 10-cm cylindrical phantom. The sum coincidences represent the total over all nine valid bankpairs, the calculator rates represent the output of the single position calculator, and the sinogram rates represent only the true coincident events, after energy gating, distortion removal, rebinning, scatter and random subtraction.

12. Ratefactor vs. average singles countrate per detector, for UGM PENN-PET scanner, for two cylindrical phantoms; 1.05 liter and 3.71 liter. The ratefactor = 1 / (1-deadtime). This curve is used to perform deadtime correction for studies, based upon the measured singles countrates.

13. Comparison between the measured activity concentration (after deadtime correction) and true activity concentration, as a function of activity in the FOV.

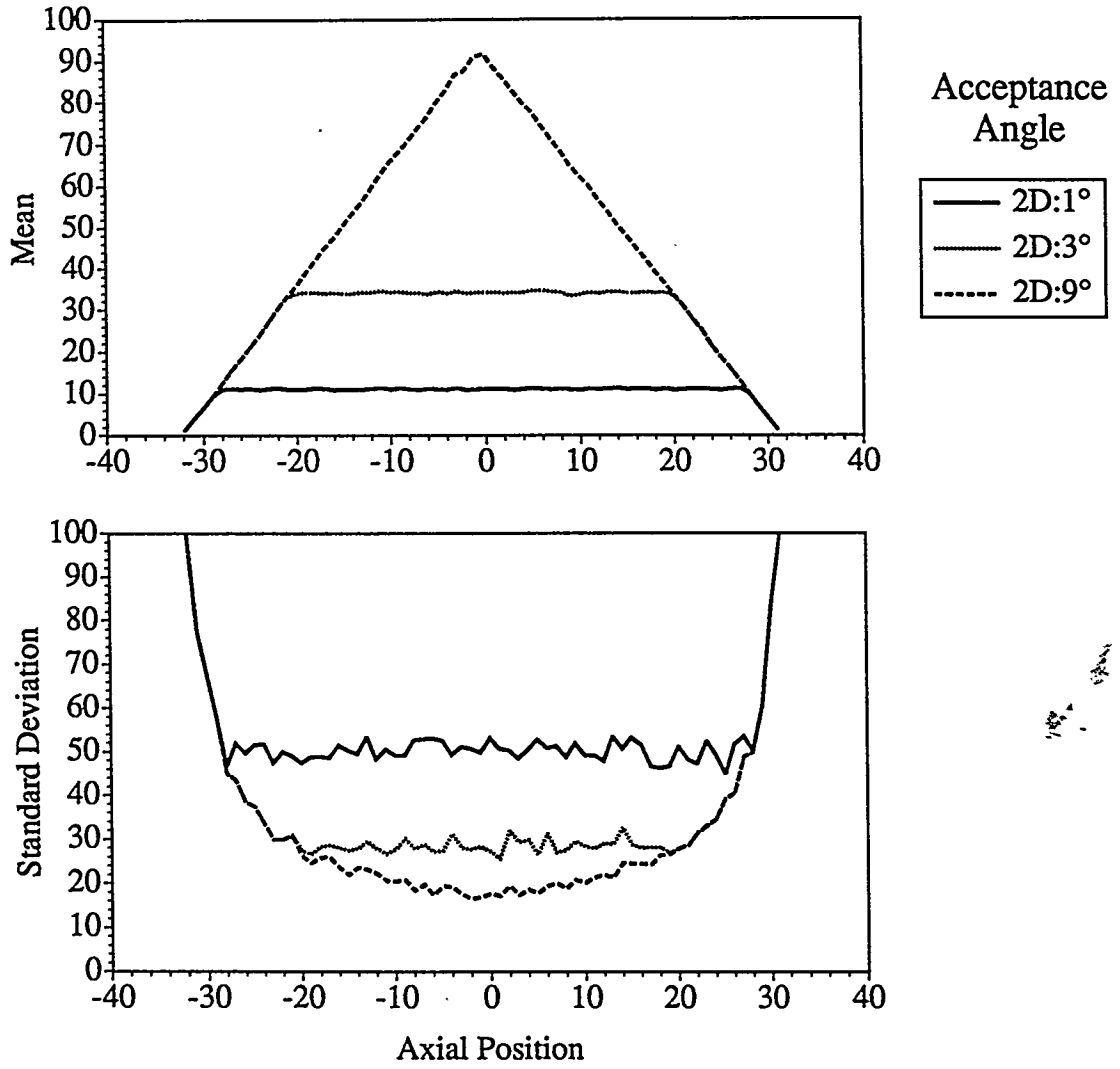
Mean
Standard Deviation
Axial Position
Acceptance Angle
2D:1°
2D:3°
2D:9°

Figure 1

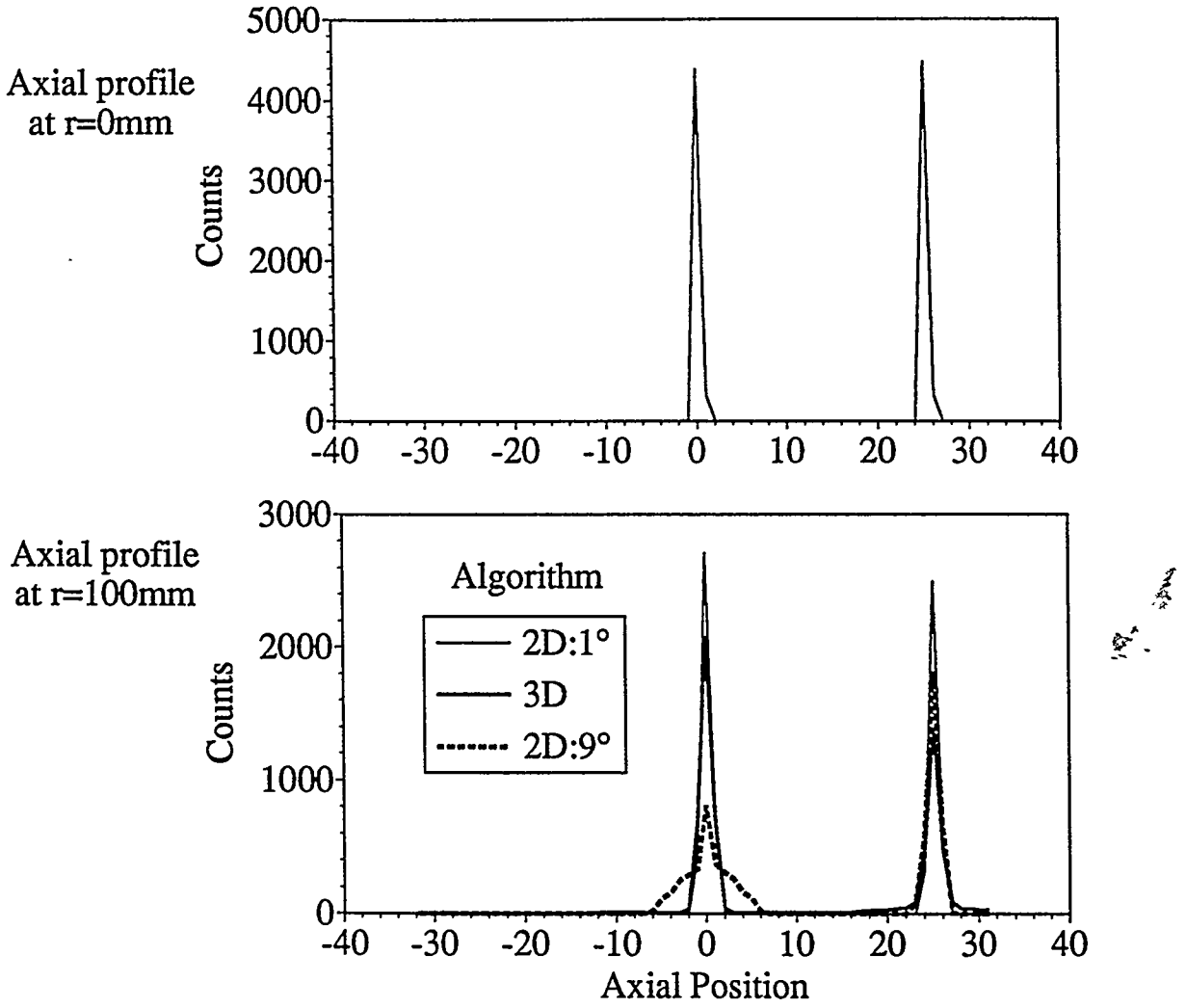
Axial profile
at r=0mm
Counts
5000
4000
3000
2000
1000
0
-40
-30
-20
-10
0
10
20
30
40
Axial profile
at r=100mm
Counts
3000
2000
1000
0
Algorithm
2D:1°
3D
2D:9°
-40
-30
-20
-10
0
10
20
30
40
Axial Position

Figure 2

Profiiles through reconstructions of disks phantoms

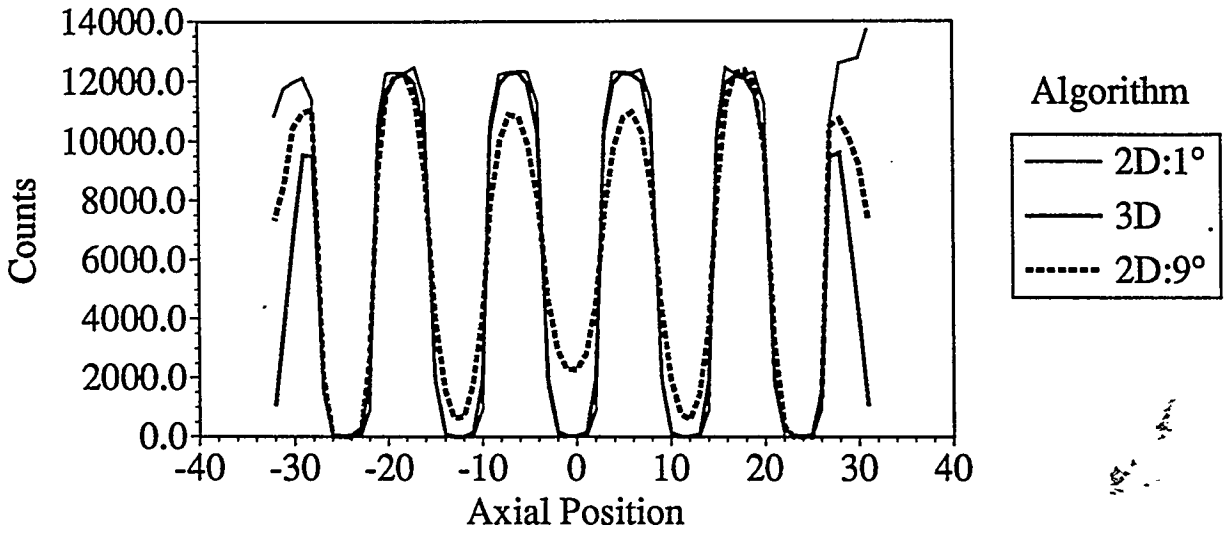

Figure 3

RMS differences of reconstructions from base image for inner, outer, and global ROIs

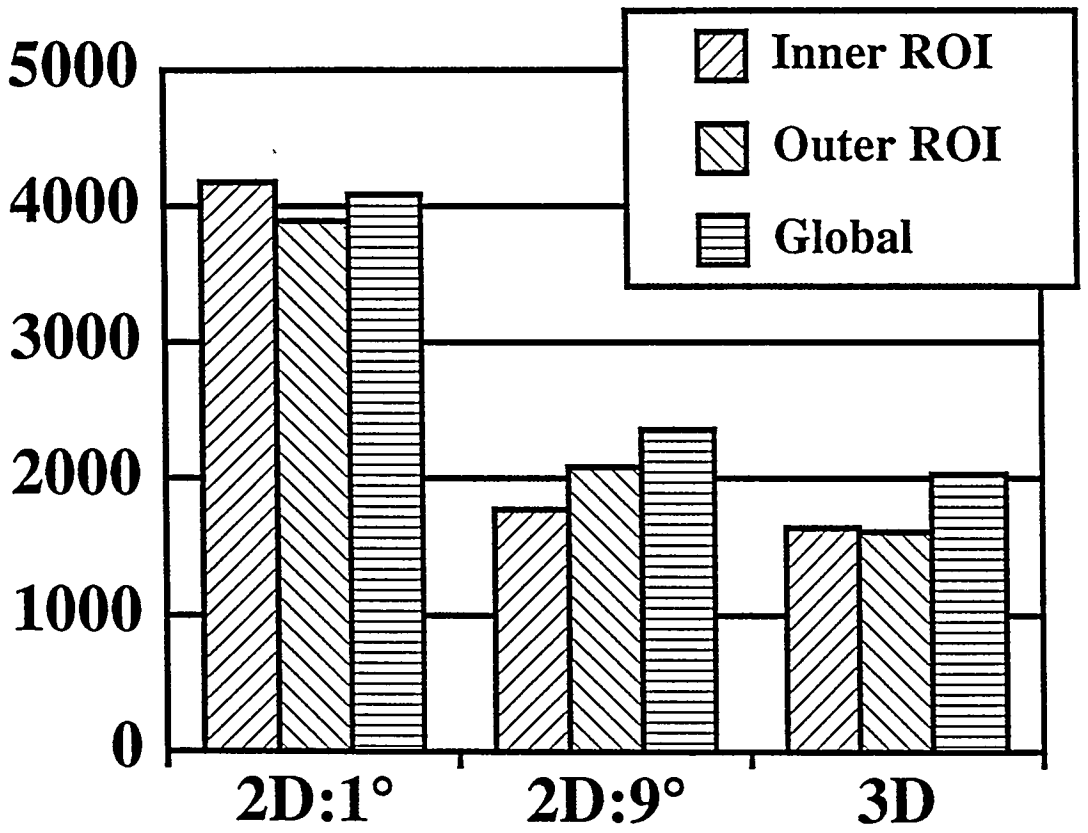

igure 4

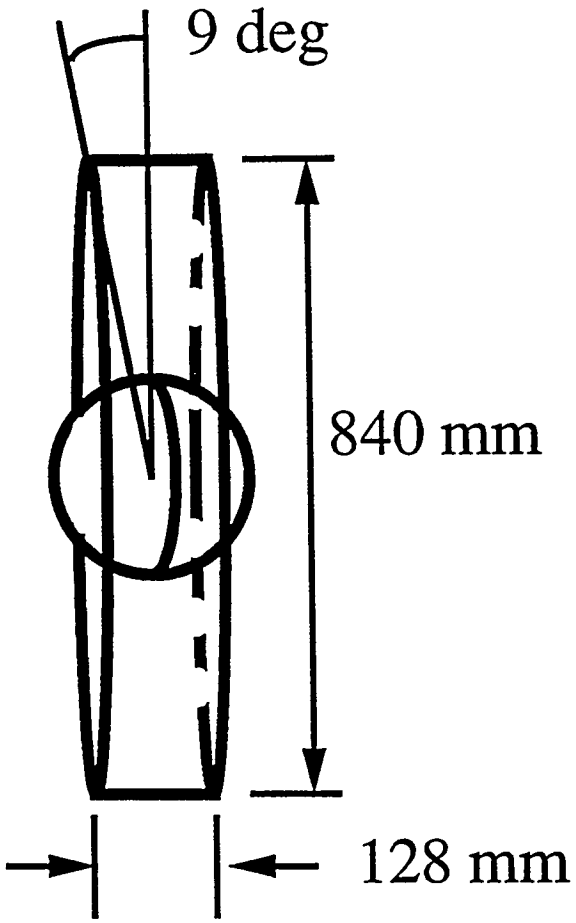

Standard Geometry

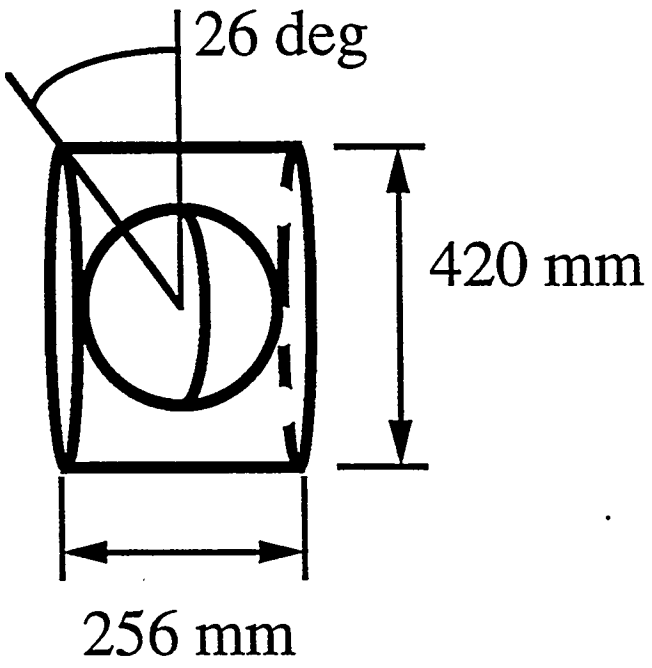

HEAD Geometry

Figure 5

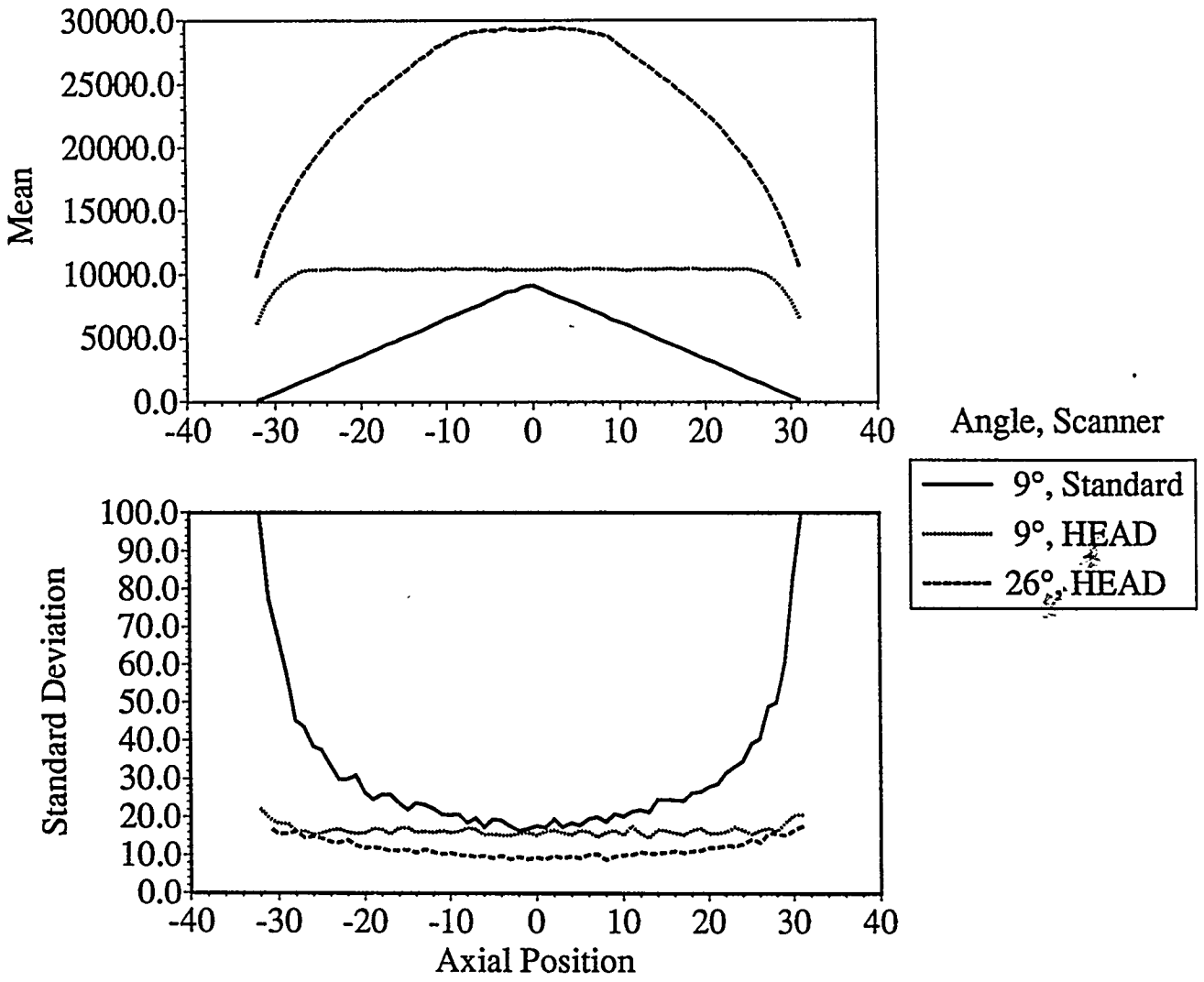
Mean
30000.0
25000.0
20000.0
15000.0
10000.0
5000.0
0.0
-40
-30
-20
-10
0
10
20
30
40
Standard Deviation
100.0
90.0
80.0
70.0
60.0
50.0
40.0
30.0
20.0
10.0
0.0
Axial Position
Angle, Scanner
9°, Standard
9°, HEAD
26°, HEAD

Figure 6

RMS differences of reconstructions from base image

3M total events

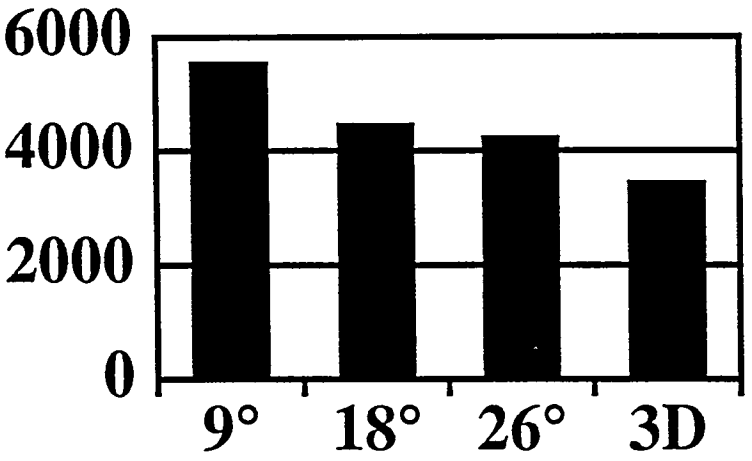

26M total events

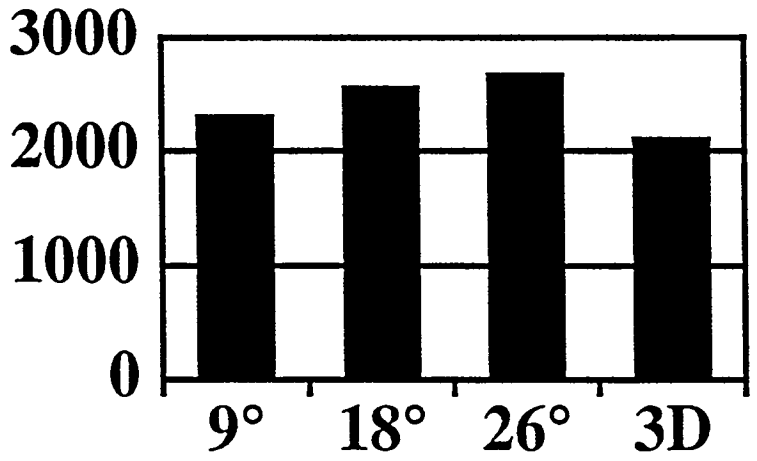

Figure 7

Simulated data with Monte Carlo program

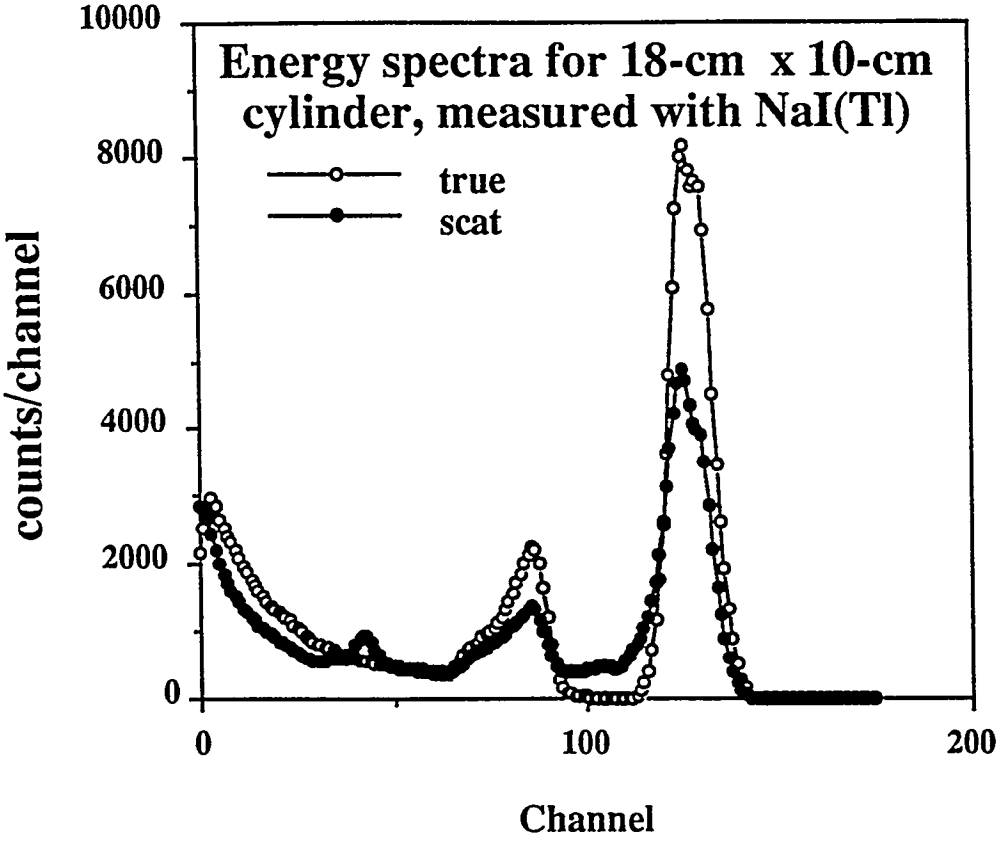

Measured data with proto-type PENN-PET scanner

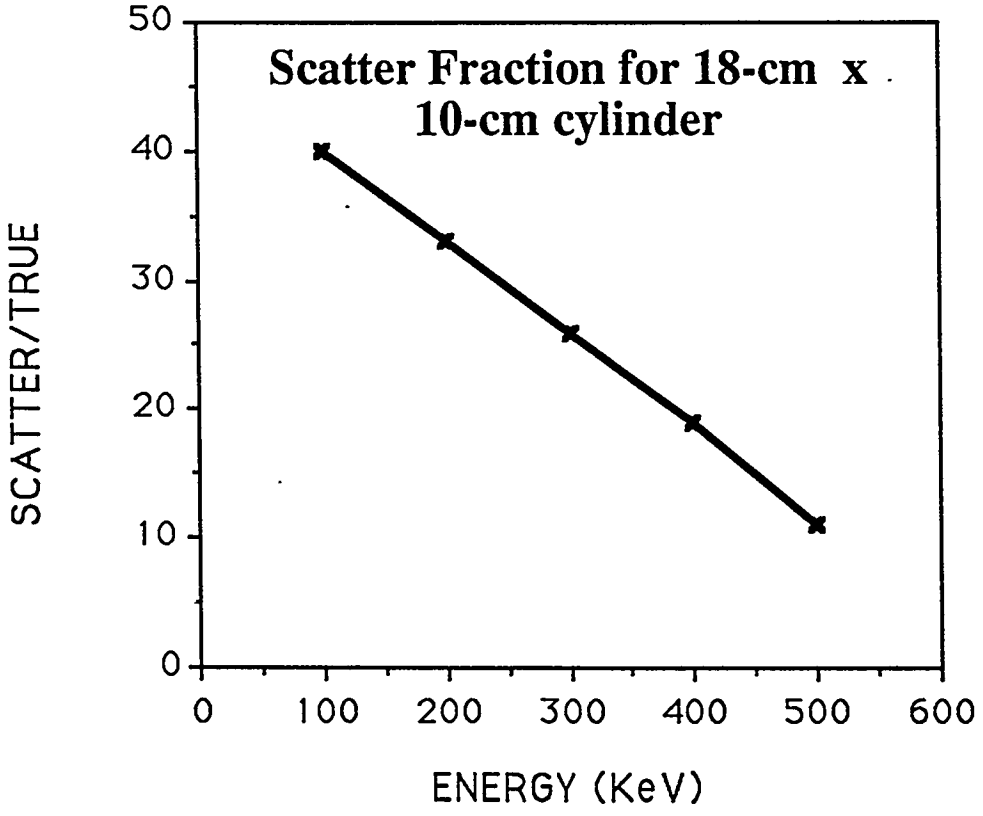

Figure 8

Simulation results

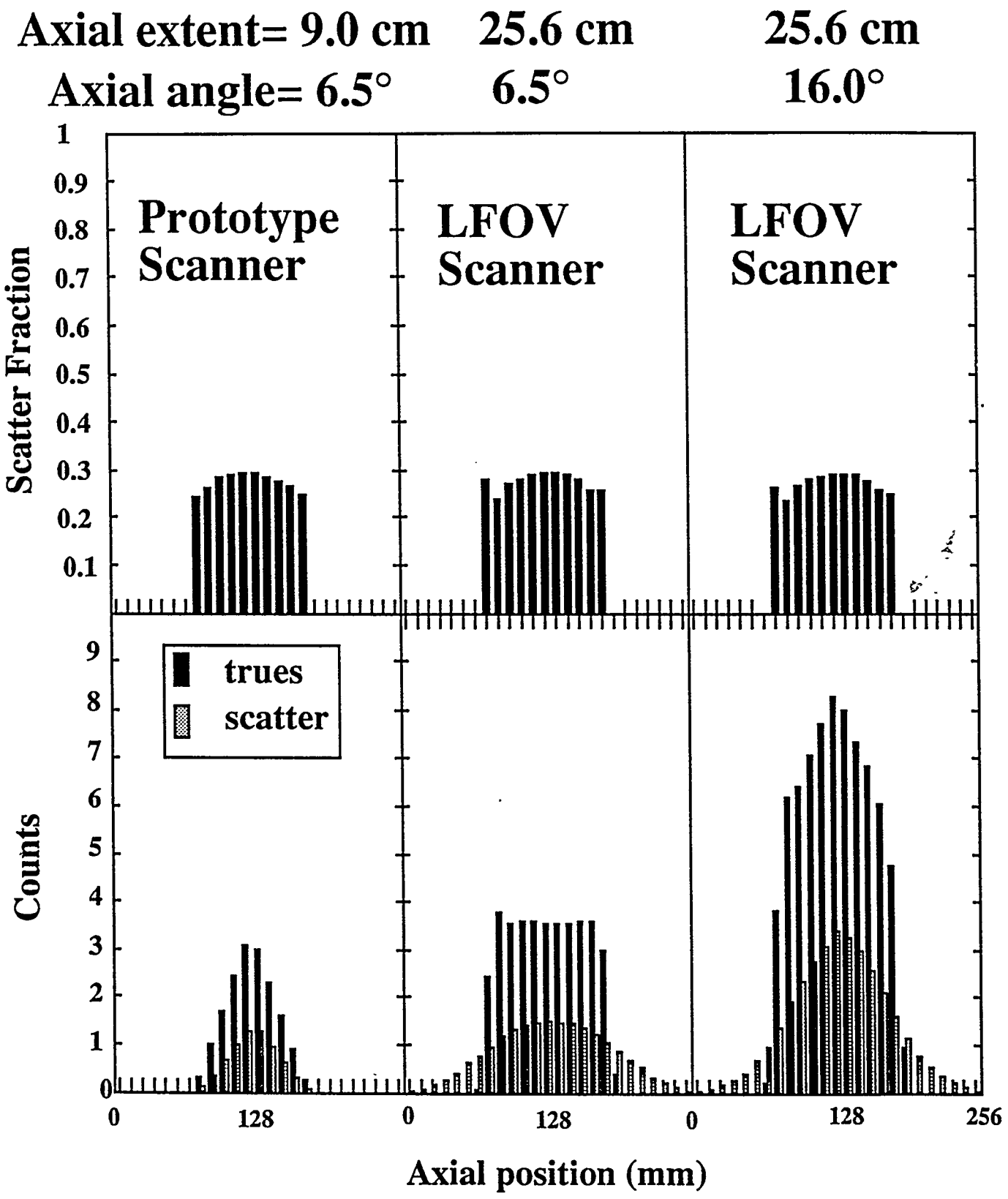

Figure 9

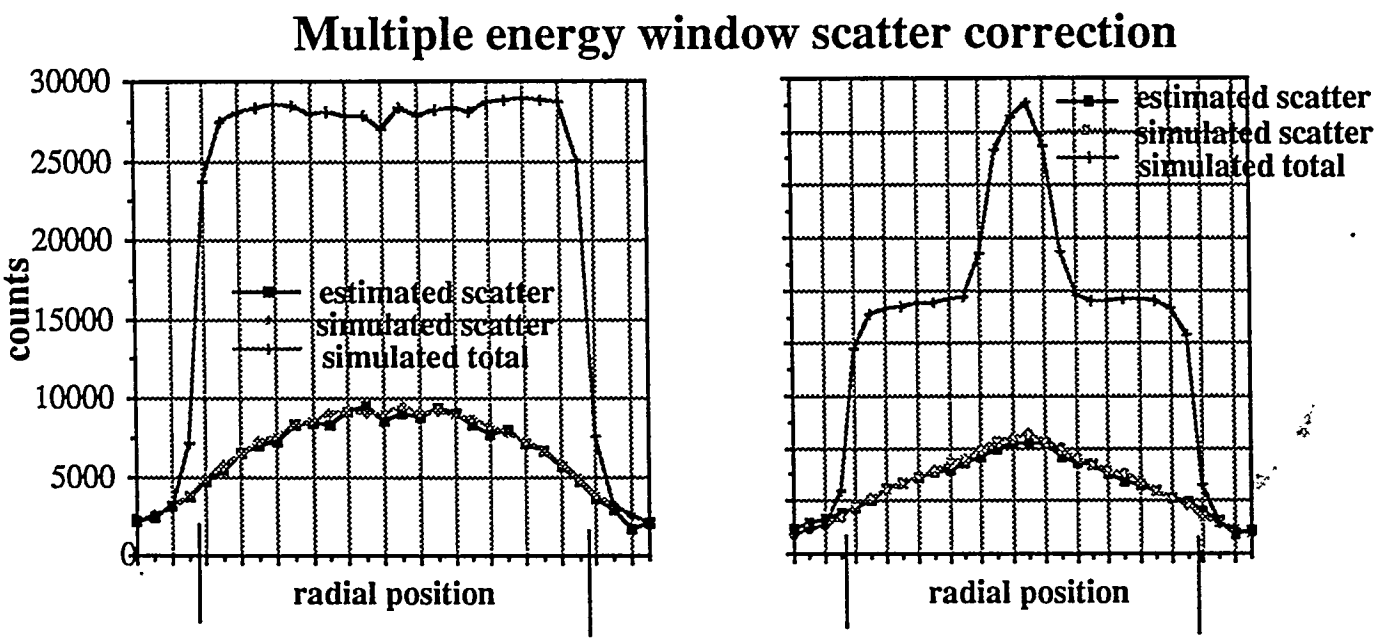

Projection profiles for a 18x10 uniform hot phantom

Projection profiles for a 10x10 cm hot cylinder in a 18x10 cm warm cylinder background (activity ratio 5:1)

Figure 10

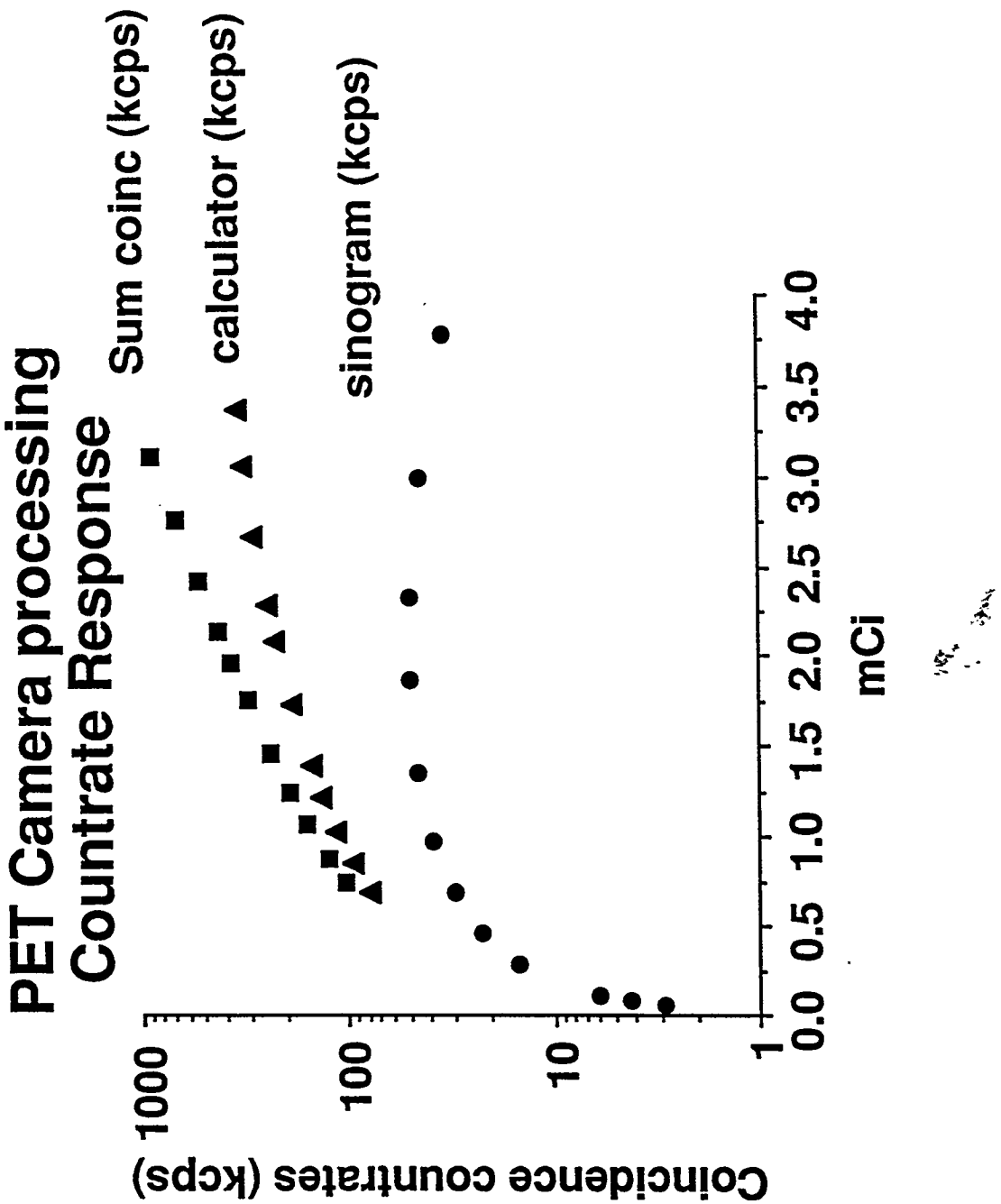
PET Camera processing
Countrate Response
Sum coinc (kcps)
calculator (kcps)
sinogram (kcps)
Coincidence countrates (kcps)
1000
100
10
1
0.0 0.5 1.0 1.5 2.0 2.5 3.0 3.5 4.0
mCi

Figure 11

Figure 12

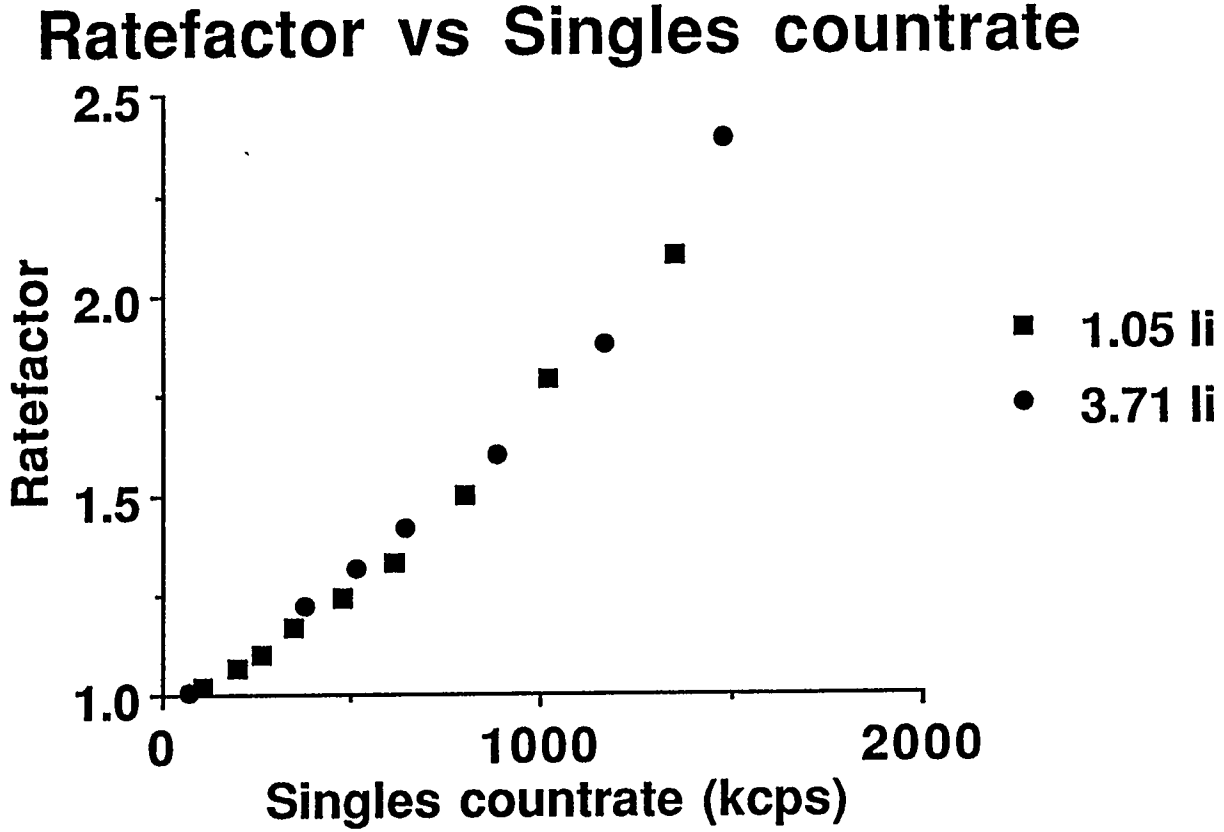

μCi/ml = Ratefactor * cpm/voxel * 1/170
sensitivity is 170 $\pm$ 6 cpm/voxel/μCi/ml

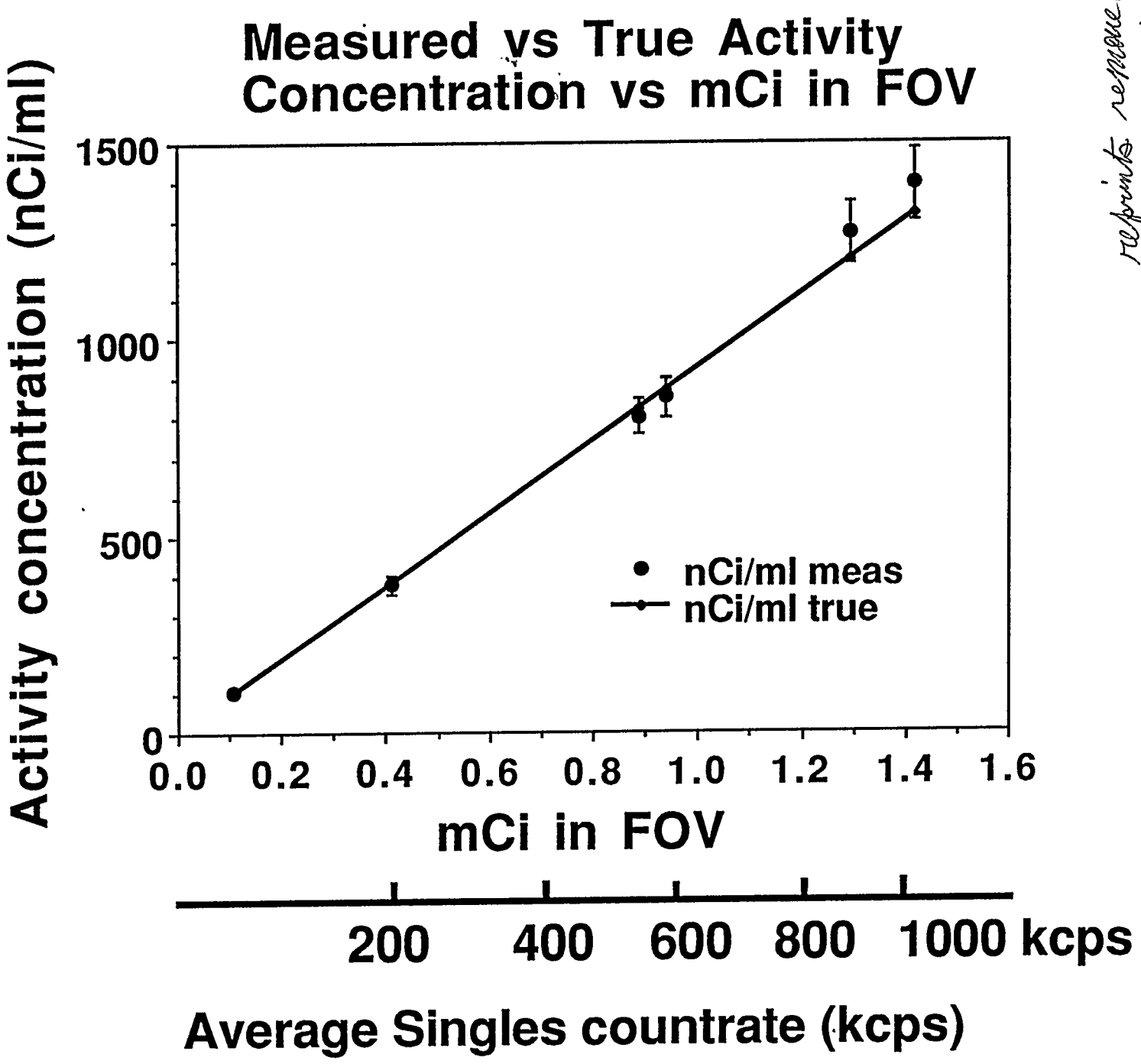

reprints removed. cbr

Figure 13